

Vacuum-UV photodesorption from compact Amorphous Solid Water : photon energy, isotopic and temperature effects

J.-H. Fillion¹, R. Dupuy¹, G. Féraud¹, C. Romanzin², L. Philippe¹, T. Putaud¹, V. Baglin³, R. Cimino⁴, P. Marie-Jeanne¹, P. Jeseck¹, X. Michaut¹ and M. Bertin¹

¹ Sorbonne Université, Observatoire de Paris, Université PSL, CNRS, LERMA F-75005 Paris
e-mail: jean-hugues.fillion@sorbonne-universite.fr

² Institut de Chimie Physique, UMR8000 CNRS, Université Paris-Saclay, 91405, Orsay, France

³ CERN, CH-1211 Geneva 23, Switzerland

⁴ Laboratori Nazionali di Frascati (LNF)-INFN I-00044 Frascati, Italy

Received XXXX, 2019; accepted XXXX, XXXX

ABSTRACT

Context. Vacuum-UV (VUV) photodesorption from water-rich ice mantles coating interstellar grains is known to play an important role on the gas-to-ice ratio in stars and planets formation regions. Quantitative photodesorption yields from water ice are crucial for astrochemical models.

Aims. The aims is to provide the first quantitative photon-energy dependent photodesorption yields from water ices in the VUV. This information is important for the understanding of the photodesorption mechanisms and to account for the variation of the yields under interstellar irradiation conditions.

Methods. Experiments have been performed on the DESIRS beamline at the SOLEIL synchrotron facility (St Aubin, France), delivering tunable VUV radiation, using the ultra-high SPICES (Surface Processes and ICES) vacuum chamber. Thick compact amorphous solid water ice (H₂O and D₂O) grown onto a cold Au substrate have been irradiated from 7 to 13.5 eV. Quantitative yields have been obtained by detection into the gas phase with mass-spectrometry for sample temperatures ranging from 15 K to 100 K.

Results. Photodesorption spectra of H₂O (D₂O), OH (OD), H₂ (D₂) and O₂ peak around 9-10 eV and decrease at higher energies. Average photodesorption yields of intact water at 15 K are 5×10^{-4} molecule/photon for H₂O and 5×10^{-5} molecule/photon for D₂O over the 7-13.5 eV range. The strong isotopic effect can be explained by a differential chemical recombination between OH (OD) and H (D) photofragments originating from lower kinetic energy available for the OH photofragments upon direct water photodissociation and/or possibly by an electronic relaxation process. It is expected to contribute to water fractionation during the building-up of the ice grain mantles in molecular clouds and to favor OH-poor chemical environment in comet-formation regions of protoplanetary disks. The yields of all the detected species except OH (OD) are enhanced above (70 ± 10) K, suggesting an ice restructuring at this threshold temperature.

Key words. interstellar medium, protoplanetary disks, ices, photodesorption, vacuum ultraviolet

1. Introduction

The photodesorption from water ice by Vacuum-UltraViolet (VUV) photons ($\lambda < 200$ nm) is known to play an important role in variety of astrophysical cold environments ranging from star and planets formation regions of the Interstellar Medium (ISM) to icy bodies of the solar system. The desorption induced by VUV photons is a non-thermal process, allowing atoms and molecules to be ejected into the gas phase from low temperature ices, especially below their condensation temperature. In the ISM, this phenomenon can deeply affect the gas-to-ice ratio in cold environments. Astrophysical models have shown that photodesorption from external stellar VUV radiation (6-13.6 eV) can prevent the formation of the water ice mantle at the surface of dust grains located at the edge of molecular clouds and supply most of the gas phase water abundance at intermediate depths into the cloud (Hollenbach et al. 2009; Furuya et al. 2015). Deeper inside molecular clouds, the secondary VUV radiation induced by cosmic rays, although 10^3 times less intense than the interstellar standard radiation field governing the photochemistry at the edge of molecular clouds, is a non-thermal desorption agent (Caselli et al. 2012), along with the desorption

induced by exothermic chemistry from grains at the very early stages of the cloud formation (Cazaux et al. 2016). The desorption directly induced by cosmic ray impact onto icy grain mantles is also strongly contributing to these non-thermal phenomena (Dartois et al. 2015, 2018). Non-thermal desorption are believed to play an important role in protoplanetary environments by maintaining molecules into the gas phase in the surface or intermediate regions of the disk (Aikawa & Herbst 1999; Willacy & Langer 2000). Dupuy et al. (2018) recently highlighted the efficient role played by soft X-ray photons to induce the non-thermal desorption of neutral water from water ice. In the comet formation region of the disk, VUV photodesorption from cold grains is supposed to be a source of reactive species, such as OH, which alter drastically the gas phase chemical composition (Chaparro Molano & Kamp 2012). Knowing the nature and photodesorption yields of the desorbing photofragments is therefore of primary importance. Moreover, VUV photodesorption of water at the disk surface, followed by recondensation to lower heights in the disk has been proposed to be at the origin of the amorphous structure of the ice in the outer solar nebula (Ciesla 2014). Strong VUV radiation may also affect deeply the water

ice distribution by pushing the snow line farther into the disk midplane (Terada & Tokunaga 2017). In the outer part of protoplanetary disks, chemical models show that most of the water is released into the gas phase through VUV photodesorption and can explain an enhancement of water vapor (Walsh et al. 2010). In the disk of the young star TW Hydrae, photodesorption is considered as the dominant form of desorption in cold unshielded regions where thermal desorption can be totally neglected (Fogel et al. 2011; Salinas et al. 2016). Consequently, water lines emission from this object are sensitive to the absolute photodesorption yields employed in the disk model (Kamp et al. 2013). Finally, photodesorption of water has also been considered to explain the ortho-to-para ratio (OPR) observed from water emission lines around TW Hydrae (Hogerheijde et al. 2011; Salinas et al. 2016) or in the Orion photon dominated region (Putaud et al. 2019).

In the laboratory, numerous water photodesorption experiments have been performed since the pioneering studies of Westley et al. (1995b,a). Öberg et al. (2009) have studied the dependence of a number of physical parameters on the H₂O and D₂O photodesorption yields, such as ice thickness, ice temperature and morphology, VUV photon flux and fluence. In these experiments, absolute yields were derived from the water ice depletion measured in the solid phase, using reflection-absorption IR spectroscopy. Cruz-Diaz et al. (2018) have reported new measurements of UV-photodesorption from H₂O and D₂O ices using a calibrated quadrupole mass spectrometer in order to detect directly, into the gas phase, intact water together with photofragments and other species formed by surface photochemistry. In all the above mentioned experiments, VUV photons were generated using a low pressure microwave-powered plasma source of H₂, producing an emission spectrum peaking at atomic H-Lyman- α (10.2 eV) superimposed on a continuum of molecular emissions (6 -11 eV) dominated by a large Lyman band of H₂ (B ¹ Σ_u^- - W ¹ Σ_g^+) centered at 7.8 eV (Es-sebbar et al. 2015; Muñoz Caro & Schutte 2003). Beside the above broadband excitation studies, the photodesorption from water ice films has also been studied at various selected energies using monochromatic sources. Experiments most probably involving multiphoton excitation processes have been carried-out using intense nanosecond laser pulses in the visible UV-range (Nishi et al. 1984; Bergeld & Chakarov 2006). Direct excitation in the VUV at 9.8 eV (126 nm) and 7.2 eV (172 nm) have also been explored using Ar and Xe excimer lamps (Watanabe et al. 2000). More recently, the investigation of water photodesorption in the VUV using excimer lasers at 6.4 eV (193 nm) and 7.9 eV (157 nm) coupled to a direct probe of the ejected species by Resonance Enhanced Multiphoton Ionisation (REMPI) have provided much insights on the desorption mechanisms from amorphous solid water at 100 K. Yabushita et al. (2013) have reviewed these experimental results. Similar experiments, with slightly different conclusions on the kinetic energy released, have also been performed on thick water ice (DeSimone et al. 2013; DeSimone & Orlando 2014) and compared to photodesorption from thinner Amorphous Solid Water (ASW) layers deposited on lunar substrates (DeSimone et al. 2013; DeSimone & Orlando 2015). All the above results could be faced to a valuable series of results from molecular dynamics simulations studying the desorption events from ASW at low (10 K) and high temperature (90-100 K), which originate from initial photodissociation in the 7-9 eV energy range (Andersson & van Dishoeck 2008; Arasa et al. 2010; Andersson et al. 2011). These studies include desorption from samples with different morphologies (amorphous vs crystalline) (Andersson et al. 2005, 2006; Crouse

et al. 2015) and isotopic effects studies (Arasa et al. 2011; Konig et al. 2013; Arasa et al. 2015).

The various excitation energies used in all these studies make direct quantitative comparison of the desorption yields difficult, because the way different excited states behave with respect to desorption is largely unknown. It has been shown, in the case of weakly bound species, that photodesorption yields can indeed be strongly energy-dependent (Fayolle et al. 2011, 2013; Bertin et al. 2013; Fillion et al. 2014; Dupuy et al. 2017). Hydrogen discharge lamps are well-suited to simulate the secondary VUV emission induced by cosmic rays inside dense molecular clouds and provide good estimate of the average desorption yields. However and despite the numerous experimental and theoretical studies mentioned above, no investigation of the desorption yields and mechanisms in the 10-13.5 eV range have been reported, though these energies could contribute to the desorption at the edges of molecular clouds or in protoplanetary disks. In order to model a specific region of space, one should ideally use monochromatic photodesorption yields weighted by the prevailing local VUV fields, but there is a lack of information concerning the photon-energy dependence of the photodesorption yields from water ice.

In this study, the photodesorption from compact ASW grown at 100 K has been investigated using synchrotron radiation enabling VUV irradiation from 7 to 13.5 eV for sample temperatures ranging from 15 K to 100 K. Water and desorbed photofragments are detected directly into the gas phase by mass spectrometry. The behavior of H₂O and D₂O pure ice samples under irradiation are systematically compared at various sample temperatures ranging from 15 K to 100 K, with the aim to provide insights on the desorption mechanisms. Several possible desorption mechanisms are discussed to explain the strong isotopic effect observed. The absolute desorption yields are compared to previous studies and astrophysical implications are discussed in the last section.

2. Methods

Experiments are performed in the SPICES (Surface Processes & ICES) set-up developed at Sorbonne Université and Observatoire de Paris (France). This apparatus has been described in detail previously (Doronin et al. 2015). It consists of an Ultra-High Vacuum (UHV) analysis chamber (10⁻¹⁰ mBar) containing a polycrystalline gold surface mounted on a rotatable cold head that can be cooled down to 15 K using a closed cycle helium cryostat. Ices of H₂O and D₂O (high purity, liquid chromatography standard from Fluka) are prepared by exposing the cold surface at 100 K to a partial pressure of gas using a tube positioned a few millimeters away from the surface, allowing growth of about 20 ML of compact Amorphous Solid Water (c-ASW) without increasing the chamber pressure to more than a few 10⁻⁹ mBar (Fillion et al. 2009). When D₂O is used, the experiment is flushed with 5×10⁻⁸ mbar of D₂O vapour during 20 minutes in order to saturate the walls with deuterium and thus avoid isotopic exchanges. The D/H purity is finally checked using Reflection Absorption Infrared Spectroscopy (RAIRS), with which O-D and O-H stretching bands of the deposited ices can be distinguished. Once the sample is condensed, the tube is moved away from the surface and the surface is rotated back towards the detector and the photon beam. Sample temperature can then be varied from 15 K to 100 K to probe the temperature effect on the photodesorption yields, while the ice is expected to keep its compact structure. Ice thicknesses are controlled with a precision

better than 1 monolayer (ML) via a calibration using the temperature programmed desorption (TPD) technique, as detailed in Doronin et al. (2015). The release of species into the gas phase is monitored by means of a Quadrupole Mass Spectrometer (QMS, model QMS200, Balzers).

The SPICES set-up has been coupled to the undulator-based DESIRS (Dichroïsme Et Spectroscopie par Interaction avec le Rayonnement Synchrotron) beamline (Nahon et al. 2012) at the SOLEIL synchrotron facility (St Aubin, France) which provides monochromatic, tunable VUV light for irradiation of our ice samples. Higher harmonics of the undulator are suppressed using a Krypton gas filter, after which the beam is directly reflected toward the ice sample. The sample is placed out of the focus plane of the beamline spot in order to get an irradiated surface area of about 1 cm² on the sample. The window-free coupling of the set-up to the beamline enables investigations up to 13.6 eV, a well-known cut-off of interstellar VUV photons due to the ionization of Hydrogen. This setting yields very stable harmonic-free photon fluxes of 10^{14–15} photons.cm⁻².s⁻¹ in a 1 eV bandwidth (Nahon et al. 2012).

To acquire Photon-Stimulated Desorption (PSD) spectra, the relative amount of photodesorbed molecules are recorded by the QMS at each selected energy from 7 to 13.5 eV by steps of 0.5 or 1 eV. Each photon energy irradiation lasts about 20 s (shutter ON) which is sufficiently longer than the dwell time of the QMS (0.5 s). Each irradiation period is followed by 30 s acquisition without irradiation (shutter OFF) in order to measure the background level on each mass. The photon energies are successively scanned using an arbitrary order, with the aim to avoid any bias linked to the evolution of the sample composition with photon fluence. An average value is extracted when the same photon energy is probed several times. Photon fluxes are measured using a Si photodiode (SXUV-100, IRD), and varies from 1.5 × 10¹⁵ photons.s⁻¹.cm⁻² at 7 eV (where the absorption cross sections are extremely small) to 2 × 10¹⁴ photons.s⁻¹.cm⁻² above 10 eV (where the ice absorption cross sections increase significantly). Under these conditions, the average total photon fluence received by the sample at the end of a typical scan is ≤ 6 × 10¹⁶ photons.cm⁻². PSD were performed for different substrate temperatures ranging from 15 K to 100 K.

Once corrected from the background contribution and divided by the photon flux, the QMS signal I_i of a species i is converted to absolute photodesorption yields at each photon energy. Absolute yields are calibrated against the well-known CO photodesorption yields (Fayolle et al. 2011). Thus, in the case of H₂O, we get:

$$Y(H_2O) = f_{CO} \times \frac{\sigma(H_2O^+/H_2O)}{\sigma(CO^+/CO)} \times \frac{F(H_2O)}{F(CO)} \times I_{H_2O}$$

where f_{CO} is the calibration factor for CO obtained with the same experiment and the same relative position of the different elements (sample, photon beam, QMS), $\sigma(i^+/i)$ is the partial electron-impact ionization cross-section of the ion relatively to its parent molecule, $F(i)$ is the apparatus function of our QMS for species i ($F(CO)$ is set to 1). These two correction factors take into account the molecular dependence of the efficiency by the ionization chamber in the QMS head, and the intrinsic apparatus function of our QMS. For others species, the signal at a given m/z ratio is corrected, when relevant, from the contribution of fragments ions originating from dissociative electron-impact ionization into the QMS head of heavier species. For example, OH signal is corrected from the cracking of the photodesorbed H₂O into OH⁺ in the ion source of the mass spectrometer. This

correction is made by considering the photodesorbed H₂O signal, from which the OH⁺ cracking signal can be estimated using the mass filter apparatus function and the dissociative electron impact ionization cross section of OH⁺ from H₂O given by Straub et al. (1998).

The absolute photodesorption yields uncertainties originate from several sources. One source of uncertainty is linked to the amplitudes of noise of the (photo)desorption and background signals respectively, that is the signal-to-noise ratio. This uncertainty is taken into account and characterized by the error bars plotted in the figures, giving that way the range of the photodesorption yields measured with equal probability. A second source of uncertainty originates from the calibration procedure. This includes the uncertainties associated to the ionisation cross sections, that of the apparatus function of the mass spectrometer, and the uncertainty associated with the calibration of the incident photon flux. We estimate that overall, the uncertainty on the absolute values related to the calibration procedure amounts to ±50%. This illustrates how difficult is the determination of absolute photodesorption yields from the experiment. Finally, a third source of uncertainties can be associated to the possible structural and chemical evolutions of the sample during irradiation, since in this experiment the sample can't be renewed between each data point. This last source of uncertainty has been estimated for each desorbing species and will be discussed in the result section.

3. Results

Figure 1.a presents the energy dependence of H₂O photodesorption yields, hereafter called Photon-Stimulated Desorption spectra, from 7 to 13.5 eV obtained at 15 K and 100 K respectively. For comparison, Fig. 1.b shows the absolute VUV absorption cross section of pure H₂O ice deposited at 8 K from 7.5 to 10.2 eV (Cruz-Diaz et al. 2018). In order to get information at higher energies, part of the absorption spectrum calculated from the reflectivity spectrum of amorphous ice at 80 K (Kobayashi 1983) has been rescaled on the same plot. In the gas phase, the absorption spectrum is characterised by two very broad absorption features centered around 7.4 eV and 9.7 eV associated to the $3s4a_1 \leftarrow 1b_1(\tilde{A}^1B_1 \leftarrow \tilde{X}^1A_1)$ and the $3s4a_1 \leftarrow 3a_1(\tilde{B}^1A_1 \leftarrow \tilde{X}^1A_1)$ transitions respectively. They are the starting point of intense and sharper transitions toward series of bent/linear Rydberg states observed above 10 eV (Fillion et al. 2001). In the solid ice, taking a band picture view and comparing with the more structured spectra of hexagonal ice, these two excited states can also be described as Frenkel-type excitons lying below the conduction band with transitions at 8.5 eV and around 10.2 eV respectively (cf Fig. 1), and with an associated ionization continuum starting around 11 eV (Kobayashi 1983).

The comparison of the figures shows that the H₂O PSD spectra do not simply mimic the absorption cross sections variations with photon energy. The PSD and absorption spectra present similar energy threshold (around 7 eV) but the first band peaking at 8.5 eV in the absorption spectrum is not observed in the PSD spectra. This can be due to experimental spectral resolution limitation, because the bandwidth of the incident radiation and that of the absorption band are similar (~ 1 eV). The desorption yields are maxima around 10 eV, corresponding to the shoulder on the absorption spectrum assigned to the second exciton band (Kobayashi 1983). PSD and absorption spectra however, clearly deviate at higher energies (> 10 eV), for which the yields continue to decrease with photon energies despite significantly higher absorption cross sections above 10 eV (Fig. 1a).

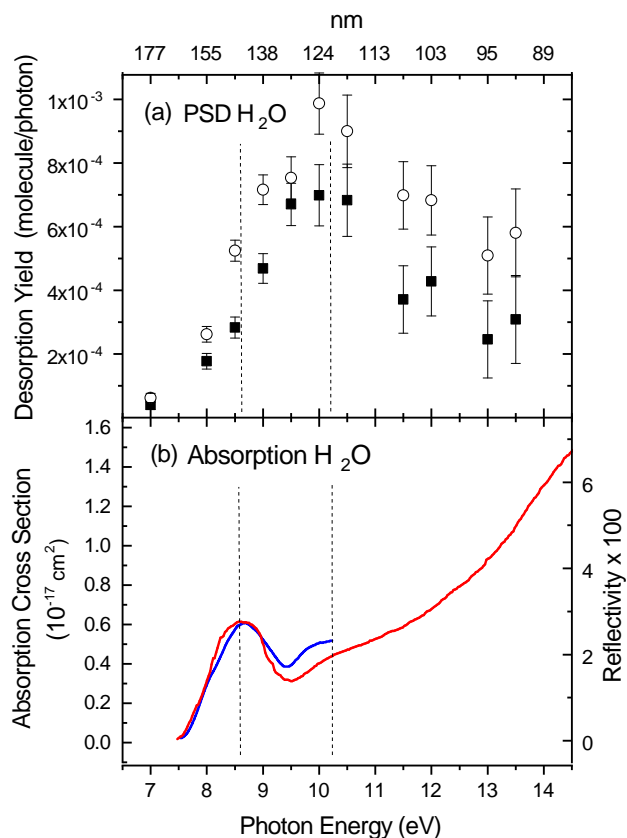


Fig. 1. (a) Photodesorption yields (molecule per incident photon) of intact H_2O at 15 K (black squares) and at 100 K (open circles) from 20 ML of c-ASW films (b) VUV-absorption cross sections of pure water ice deposited at 8 K from Cruz-Diaz et al. (2014b) (blue curve) and reflectivity spectrum of amorphous ice at 80 K from Kobayashi (1983) (red curve). The reflectivity spectrum has been rescaled against the absorption spectrum at 8.3 eV. The dotted vertical lines point the position of the first two excitonic bands.

A similar behavior is seen for the desorption of D_2O (from D_2O c-ASW), as shown in Fig. 2. In the first absorption band (8.75 eV), the desorption yields reach 70 % of their maximum values. The yields are maxima around 10 eV (second absorption band of the absorption spectrum). Above 10 eV again, the desorption yields of D_2O are continuously decreasing with photon energies. These effects are observed both at low (15 K) and high temperatures (100 K) for H_2O and D_2O (Fig. 1 and 2). One can note this behavior is rather different from that observed from weakly bound condensates of diatomic molecules, such as CO , N_2 or NO ices, for which PSD and absorption spectra are extremely similar in spectral regions corresponding to electronic transitions, as a signature of a Desorption Induced by Electronic Transition (DIET) process (Fayolle et al. 2011, 2013; Dupuy et al. 2017). In the present case, the deviation between PSD and absorption spectra likely results from multiple and/or less-direct desorption mechanisms at play associated with the dissociative character of the electronic excited states involved. The decrease of the photodesorption yields at high energies could result from the fact that the ionization of the sample does not contribute directly to the desorption events, whereas it contributes to the increase of the absorption cross section above the ionization threshold.

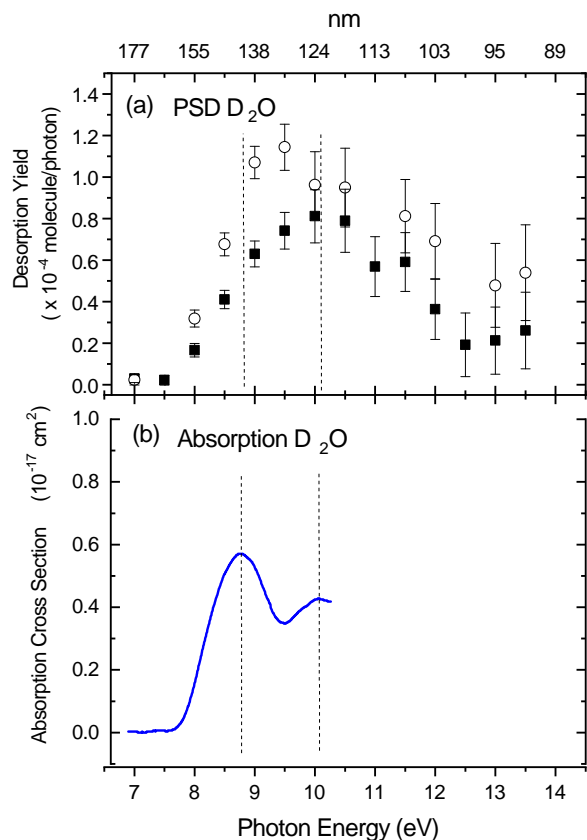


Fig. 2. (a) Photodesorption yields (molecule per incident photon) of intact D_2O (black squares) and at 100 K (open circles) from 20 ML of c-ASW films (b) D_2O absorption cross sections from Cruz-Diaz et al. (2014a). The dotted vertical lines point the position of the first two excitonic bands.

For both H_2O and D_2O , we observe no significant difference ($< 5\%$) in the intact water photodesorption yields recorded at the beginning of the measurement cycle of a PSD scan, compared to that obtained at the end. This indicates the water photodesorption yields are not evolving with photon fluence ($\leq 6 \times 10^{16} \text{ photons.cm}^{-2}$). This could be surprising considering that VUV photons may induce structural and chemical modifications of the sample. Indeed, the porosity of amorphous water ice is known to decrease with photon fluence upon VUV (or ion) irradiation (Palumbo et al. 2010). In the present case however, since the ice has been grown at high temperature, the structure of the sample is already non-porous. Following Jenniskens et al. (1995), VUV irradiation merely favours the formation of high-density ASW, affecting the relative distribution of the coordination number of the hydrogen bonds. Possible slight modifications of the local density within the ice bulk do not seem to affect H_2O and D_2O photodesorption yields in the present experimental conditions.

One major finding of the present investigation is to reveal that photodesorption is mostly efficient in the second excitonic band ($\sim 10 \text{ eV}$), a result that could not be anticipated from the absorption cross sections and from our current understanding of the mechanisms, despite previous extended investigations on water. Consequently, this result confirms, in retrospect, that excitation at Lyman- α (10.2 eV) is relevant to investigate water photodesorption in the VUV. This is again in contrast with other systems, such as CO , N_2 or CO_2 , that do not desorb efficiently at this en-

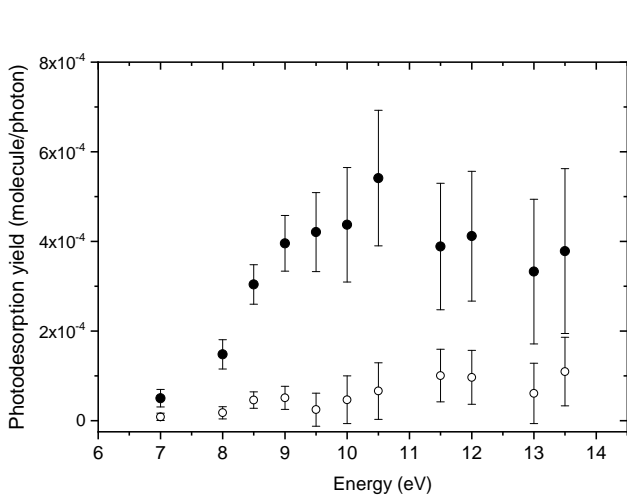


Fig. 3. Photodesorption yields of OH (open circles) and OD (full circles) from 20 ML H₂O and D₂O compact amorphous ices at 15 K.

ergy and for which hydrogen-discharge lamps optimized for this transition are not very well-suited for a quantitative determination of the photodesorption yields in the VUV.

The temperature dependences of the photodesorption yields of intact water molecules from H₂O and D₂O ices are similar. PSD spectra confirm that the desorption yields slightly increase with the sample temperature. The integrated desorption yield from 7 to 13.5 eV increases by a factor ~ 1.5 from 15 K to 100 K for both systems. This temperature dependence is weak as compared to what is observed for other molecules, as it will be shown below.

The general trends of the photodesorption yields with photon energy and temperature are very similar for both H₂O and D₂O, but their absolute values are dramatically different. Photodesorption yields of water measured at 10 eV (the maximum value over the total energy range) from 15 K c-ASW are $(7 \pm 1) \times 10^{-4}$ molecule/photon and $(8 \pm 1) \times 10^{-5}$ molecule/photon for H₂O and D₂O respectively. Considering the integrated desorption yields from 7 to 13.5 eV, this effect is characterized by the isotopic ratio $Y(\text{H}_2\text{O})/Y(\text{D}_2\text{O}) \sim 10$, independently of the sample temperature. We can therefore conclude that the desorption of H₂O is significantly enhanced as compared to its heavier isotopologue D₂O, at any photon energy and temperature. This effect can not be explained by the difference in absorption cross section between the two species since according to Cruz-Diaz et al. (2014a), H₂O absorption cross sections exceed that of D₂O by $\sim 10\%$ only at 10 eV. It must originate mainly from different weights of the various desorption channels at play producing intact water.

Figure 3 presents the photodesorption of OH and OD radicals from H₂O and D₂O ices at 15 K respectively. Contrary to the previous case, no clear dependence of the photodesorption yields with ice temperature has been observed (cf Fig. 6), and only low temperature results are shown in Fig. 3. No evolution of the photodesorption yields with photon fluence could be seen for OD nor for OH. The overall spectral shape of OD desorption seems different from that of D₂O. The OD desorption yields $Y(\text{OD})$ increase slowly with photon energy from 7 to 9 eV, reaching $(3.9 \pm 0.6) \times 10^{-4}$ molecule/photon at 9 eV. This desorption yield is maintained up to 13.5 eV. By contrast, the OH desorption yields $Y(\text{OH})$ are near the detection limit of this experiment, and if we consider the error bar, it is difficult to confirm its detection

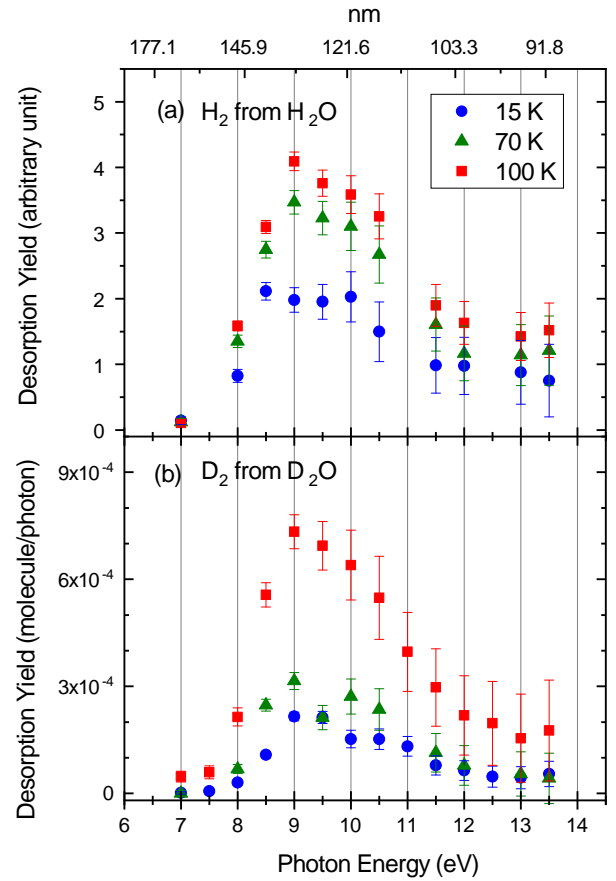


Fig. 4. Photodesorption yields of molecular hydrogen at 15 K (blue circles), 70 K (green triangles), 100 K (red squares) for (a) H₂ from H₂O (20 ML c-ASW) and (b) D₂ from D₂O (20 ML c-ASW). The desorption yields for H₂ have been arbitrary scaled.

and draw any definitive conclusion about the evolution of OH desorption yields with photon energy. We estimate OH maxima desorption yields from H₂O are $\lesssim 10^{-4}$ molecule/photon above 9 eV. By contrast to what was observed for the desorption of the parent water molecules, only the desorption yield of the heaviest radical (OD) is confidently measured, suggesting the existence of an isotopic-dependent mechanism.

Figure 4 shows the desorption of molecular hydrogen at several temperatures (H₂ and D₂ from H₂O and D₂O ices respectively). The shapes are similar to that of H₂O/D₂O desorption curves. All the desorption curves are peaking around 9 eV. This value almost matches the maximum of the first exciton band for both H₂O and D₂O. The desorption curves measured at 30 K (not shown) were similar to that observed at 15 K, but a strong enhancement of the desorption yields is observed at higher temperature. From 15 K to 100 K, the desorption yields increase significantly, e.g. by a factor of 2 and more than 3 for H₂ and D₂ respectively. A more detailed investigation of the temperature dependence follows below. We observe a slow increase of H₂ and D₂ desorption signals with photon fluence (not shown), in line with substantial surface chemistry. From the D₂ signal, we estimate this effect could account for a variation of 20% of the yields measured over the timescale needed to record a spectrum (a variation not included in the error bars). In the present experiment, the mass 2 channel lies close to the mass cutoff of the QMS, which makes the apparatus function for this channel

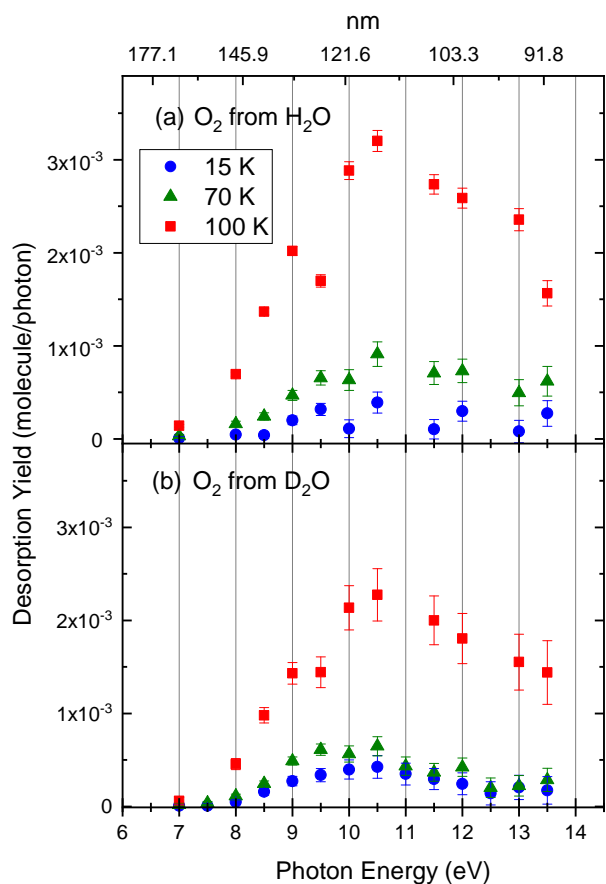


Fig. 5. (Photodesorption yields of molecular oxygen at 15 K (blue circles), 70 K (green triangles), 100 K (red squares) for (a) O_2 from H_2O (20 ML c-ASW) and (b) D_2 from D_2O (20 ML c-ASW).

rather unreliable and prevents from any comparison between H_2 and D_2 photodesorption yields.

The desorption yields of O_2 from H_2O and D_2O ices are shown and compared in Figure 5a and 5b respectively. The PSD spectra present very similar trend, with a desorption increasing with photon energy and reaching its maximum around 10.5 eV. High desorption rates are maintained at higher energies, a behavior different from that observed for H_2 (D_2). The desorption of O_2 is known to be strongly dependent on the photon fluence (Cruz-Diaz et al. 2018). We observed a non-linear increase over a long period of irradiation, without reaching any steady state after about 40 minutes of irradiation time ($\sim 10^{18}$ photons.cm $^{-2}$). Over the timescale needed to record a PSD spectrum, we observe that the O_2 production rates can increase by a factor of two. Consequently, the absolute desorption yield measured at one energy is sensitive to the number of points that have been recorded previously to its determination (i.e. to the photon fluence). Although values obtained at each energy are resulting from an average of measurements taken in random order, care should be taken on the absolute desorption values obtained here for O_2 .

Again, a significant enhancement of the desorption of O_2 with temperature is observed. In order to get more insights about the role of this parameter, we investigated in more details the temperature dependence of the desorption yields for H_2O (D_2O), H_2 (D_2) and O_2 at 10 eV. The results are shown in Figure 6. The global behavior is surprisingly very similar for all the masses, with the notable exception of the radicals OD and OH. One can

note two desorption components. A first component from 15 K to ~ 60 -80 K with nearly constant desorption yields. A second desorption component above ~ 60 -80 K, with desorption yields increasing linearly with T. Despite the fact that different mechanisms are underlying the desorption of these molecules, the behavior in the high temperature regime reveals a common source for the enhancement of the various yields.

4. Discussion

In this experiment, the desorption of H_2O (D_2O), OH (OD), H_2 (D_2) and O_2 are observed over the full energy range (7-13.5 eV). This observation is consistent with previous experimental photodesorption studies involving specific wavelengths (121.6 nm, 157 nm or 193 nm). H is known to be by far the most abundant desorbing species from the ice (Andersson & van Dishoeck 2008) but the corresponding absolute yield can not be measured with our apparatus. In the present study, we focus on quantitative photodesorption yields of the main molecular compounds following the electronic excitation within the solid sample. Among all the molecules detected, one can distinguish the desorption of water and hydroxyl radical presenting desorption channels that are partially connected to each other and for which advanced theoretical studies have been already proposed, to that of molecular hydrogen and molecular oxygen entirely associated to surface (photo)chemistry. These two sets of molecules are discussed successively below.

4.1. Desorption of intact water molecules and hydroxyl radicals

Several mechanisms have been proposed to explain the photodesorption of intact water : (1) (Electronic mechanism) excitons generated in the ice end-up localizing near the surface where the charge redistribution of the surface water molecules results in a repulsive electrostatic force (Nishi et al. 1984; DeSimone et al. 2013). (2) (Kick-out mechanism) a momentum transfer from an H atom released following water photodissociation to a surface water molecule which is ejected (Andersson & van Dishoeck 2008) (3) (Chemical recombination) desorption after recombination of H and OH fragments originating from the same water molecule (geminate recombination) (Andersson et al. 2011). Desorption after recombination at the surface of photoproducts from different water molecules (non-geminate recombination) could also be considered in addition.

Our measurements do not present time dependency of the H_2O photodesorption yields, a fact that was also shown by Öberg et al. (2009) and attested by step-like behavior of the water desorption yields upon irradiation observed by Cruz-Diaz et al. (2018), indicating that if any photochemistry is at play, it must involve fast non-thermal reactions. Translational and rotational energy measurements of photodesorbed water molecules in their ground states from ASW at 90 K after irradiation at 157 nm were found in good agreement with those predicted by MD simulations for the kick-out mechanism at 10 K (Yabushita et al. 2009; Hama et al. 2010a; Andersson et al. 2011). Another similar experiment at 108 K concluded that desorption on repulsive delocalized excitonic state was also likely to produce water in its ground state and could contribute to vibrationally excited water as well (DeSimone et al. 2013). The recombination processes, for which no measurements of the translational and rotational energy were possible, are expected to produce vibrationally excited water molecules due to the high exothermicity of the reaction (~ 5 eV). Thus, electrostatic repulsion, kick-out processes

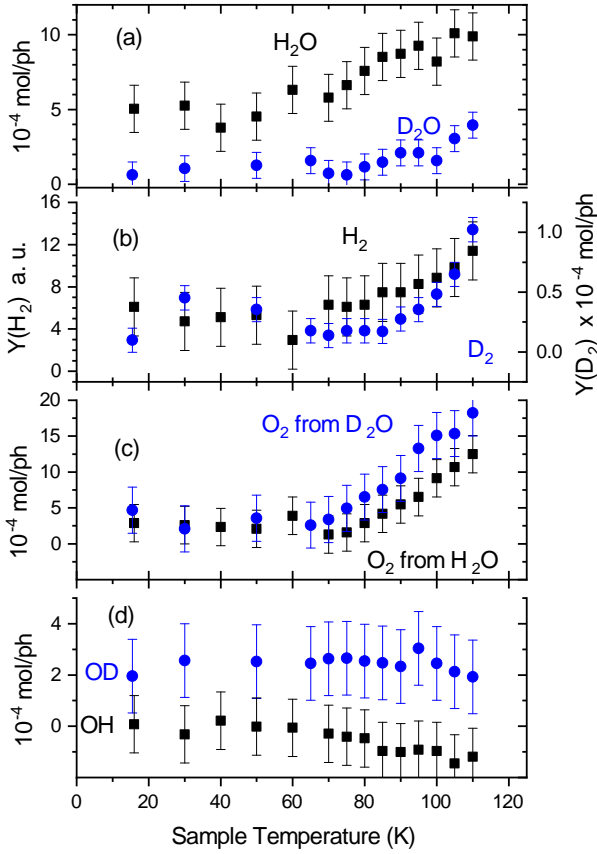


Fig. 6. Photodesorption yields from H₂O (black squares) and from D₂O (blue circles) at 10 eV as a function of the sample temperature (100 ML c-ASW); The desorbing species are : (a) water, (b) molecular hydrogen (c) molecular oxygen and (d) hydroxyl radicals.

and surface chemistry are all believed to contribute to the photodesorption yields of intact water. Andersson & van Dishoeck (2008) predict equivalent efficiency for the kick-out mechanism and geminate recombination for the desorption of intact water. In our experiment, the relative contributions of each individual mechanism to the whole desorption process, including electronic processes and non-geminate recombination (or other exothermic chemistry) are not precisely known, but will be discussed in the following.

The experiments exploring the desorption dynamics of OH radicals from ASW at 90 K following photon excitation at 7.89 eV (157 nm) have evidenced two different desorption mechanisms. The main one is characterized by non-thermal desorption (translational energy of 1300 K) due to direct water photolysis at the surface of ASW (Hama et al. 2009). The second contribution arises from secondary photodissociation of H₂O₂ at high fluence ($> 10^{17}$ photons.cm⁻²). This second mechanism is not dominant in the present study in which the fluence is more limited. Therefore, the OH photodesorption signal results mainly from the direct photodissociation of water, which is consistent with the absence of dependence with the surface temperature for this desorption channel (Fig. 6).

Molecular Dynamics (MD) calculations have investigated the photodissociation probabilities within the active top layers of the ice film. In order to compare the desorption yields (molecule/photon) of the present study to these theoretical results, we have used the probabilities of desorption (molecule per

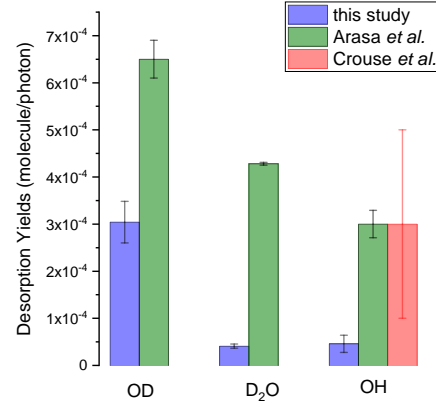


Fig. 7. Experimental photodesorption yields for 8.5 eV photons energy at 15 K (blue) compared to molecular dynamics calculations from Arasa et al. (2011) at 10 K (green) and from Crouse et al. (2015) at 11 K (red).

monolayer) P_{des}^i given by Arasa et al. (2015) in each sublayer i . The desorption yields are calculated by taking into account the probability P_{abs}^{ML} that a photon is absorbed in a given ML and the probability that the photon has not been absorbed by the overlayers. For a given desorbing species, the total photodesorption yields, following Arasa et al. (2011), are obtained by summing over the top 4 layers since the contribution from deeper layers can be neglected :

$$y = \sum_{i=1}^4 P_{des}^i (1 - P_{abs}^{ML})^{i-1} P_{abs}^{ML} \quad (1)$$

where $P_{abs}^{ML} = (1 - e^{(-\sigma N)})$ is obtained using the absorption cross sections at 8 K measured by Cruz-Diaz et al. (2014b) at the maximum of the first absorption band at 8.5 eV and taking $N = 1.1 \times 10^{15}$ cm⁻² for ASW surface density (Kimmel et al. 2001). The comparison between theoretical yields from Arasa et al. (2015) and the measured desorption yields at 8.5 eV is presented in Figure 7. Crouse et al. (2015) derived theoretical yields in a flexible water model allowing energy transfer between photofragments and the surrounding molecules. Their calculated values are shown for the non-deuterated species for comparison. One can note that calculated and experimental values lie remarkably within the same range. There are however several major differences between the experimental and theoretical values. At first, regarding the total yields $Y_D = Y(OD) + Y(D_2O)$ and $Y_H = Y(OH) + Y(H_2O)$, we observe $Y_D/Y_H = 1$ in the experiment and $Y_D/Y_H = 2$ in the calculation. The isotopic effect observed on water desorption in the calculations originates from a most efficient momentum transfer for heavier species (kick-out mechanism). Second, the distribution between OD (OH) and D₂O (H₂O) are different. In the calculation, the desorption of hydroxyl radicals slightly dominates for both species with 60% of OD and 40% of D₂O on one side and 66 % of OH and 34 % of H₂O on the other side, or are predicted similar as calculated for OH and H₂O by Crouse et al. (2015) (Fig. 7). Experimental data show an opposite behavior regarding the dominant desorption routes in the non-deuterated species, that is 88 % of OD desorption (12 % of D₂O) but ≥ 86 % of H₂O desorption (≤ 14 % of OH). This results in a very large isotopic effect in the experimental yields characterized by $Y(H_2O)/Y(D_2O) \sim 10$. The fact that $Y(H_2O)$

> $Y(\text{OH})$ is consistent with the data shown in Cruz-Diaz et al. (2018), although the absolute yields found in this latter study are higher than ours (an aspect which will be discussed below).

As mentioned earlier, the kick-out mechanism predicts an opposite behavior to that observed, with higher probabilities for the desorption of D_2O as compared to H_2O due to a better mass ratio between D and D_2O . This is a strong indication that other processes are active in the experiment.

Strong isotope effects observed in Electron Stimulated Desorption (ESD) from surfaces have been explained in the framework of Menzel-Gomer-Redhead (MGR) model (Ramsier & Yates 1991), which also applies to Photon Stimulated Desorption. In this model, the excitation onto an isotope-independent excited potential energy surface is followed by fast deexcitation to highly vibrationally excited levels of the electronic ground state. The desorption occurs when the kinetic energy gained during this sequence is large enough to overcome the ground-state desorption barrier. The model predicts an isotope effect because a lighter particle is accelerated in a shorter time on the excited Potential Energy Surface (PES) and, thus, has less probability to relax onto the ground state before reaching the critical adsorbate-substrate distance on the excited-state above which the desorption becomes energetically allowed. Quantitatively, for two species with masses m_1 and m_2 , the isotope effect is given by

$$\sigma_{m_1}/\sigma_{m_2} = (1/P_d)^{[\sqrt{m_2/m_1}-1]} \quad (2)$$

where σ_{m_1} and σ_{m_2} are the respective desorption cross sections and P_d the photodesorption probability of the mass m_1 species. Wolf et al. (1991) have applied the MGR model to the isotopic fractionation of $\text{H}_2\text{O}/\text{D}_2\text{O}$ on Pd(111) with $\sigma_{\text{H}_2\text{O}}/\sigma_{\text{D}_2\text{O}} \sim 1.4$, a process mediated by the excitation of the metallic substrate which can not be transposable here. A variation of the MGR model has been proposed by Zhu & White (1992) in order to explain the strong isotopic fractionation observed in the desorption of ammonia ($\sigma_{\text{NH}_3}/\sigma_{\text{ND}_3} \sim 4$). In this model the considered repulsive PES is along the N-H coordinate instead of the adsorbate-substrate coordinate and a strong coupling between the N-H vibration mode to the N-surface mode is assumed to allow for the energy transfer leading to desorption. Excitation of water onto a repulsive state along the HO-H coordinate appears to be well-suited with such a picture due to the dissociative character of the water excited states. Given that m_1 and m_2 are the masses of D and H atoms in this revised model, $\sigma_{\text{H}_2\text{O}}/\sigma_{\text{D}_2\text{O}}=10$ gives a probability of desorption for H_2O $P_d(\text{H}_2\text{O})=4 \times 10^{-3}$. The corresponding desorption yield depends on the number of layers contributing to the desorption. Considering equation 1 to calculate the desorption yield and $P_d(\text{H}_2\text{O})$ for each layer, it ranges from 2.6×10^{-5} molecule/photon assuming a contribution of the 4 upper layers up to 5×10^{-4} molecule/photon in the case of 20 layers. A thickness of 11 ML would match the experimental yield of 2.8×10^{-4} molecule/photon (obtained at 8.5 eV and 15 K). This value is realistic considering that electronic excitations might diffuse from the bulk to the interface (Petrik & Kimmel 2003). Nevertheless, the validity of this modified MGR model in the case of water would need to be confirmed, because it requires a full energy transfer from the intra-molecular vibrational mode toward inter-molecular vibrational mode (that is the desorption coordinate). The efficiency of such a coupling between vibrational modes is questionable. In fact, strong dipole-dipole interactions between the OH groups results in a very fast vibrational energy transfer towards other intra-molecular vibrations of the water ice network (Zhang et al. 2011) and we expect this effect to compete against desorption by favouring energy dilution

into the matrix. Assigning such huge isotope effect to this mechanism alone seems thus doubtful, especially since it has not been backed up by previous characterisations of the desorption processes listed above, all contributing to the desorption yield (Andersson et al. 2011; Hama et al. 2010b; DeSimone et al. 2013), but it cannot be completely ruled out.

The role of chemical recombination can also be discussed despite the fact that no isotopic dependence was seen in the molecular dynamics simulations for this desorption channel (Koning et al. 2013). Indeed, it is tempting to correlate the differences observed in the desorption of hydroxyl radicals to that of H_2O and D_2O desorption. The desorption of OH/OD radicals originates from a direct photodissociation event, a fact further confirmed by the lack of temperature dependence in the OD signal (Fig. 6). As pointed out by Koning et al. (2013), the probabilities of desorption of hydroxyl radicals (OH or OD) are mainly governed by their initial kinetic energy upon photodissociation. Indeed, considering an isolated water molecule, the conservation of energy and linear momentum implies that OD radicals have higher kinetic energies than the OH radicals upon water photodissociation. More precisely and following Koning et al. (2013), for an initial photon energy of 8.5 eV, the total energy available after photodissociation is $E=3.1$ eV, which after distribution between X and OX (X= H or D) photofragments and small corrections taking into account the average energy released in the vibration is partitioned as 0.275 eV and 0.142 eV of translational energy for OD and OH respectively. This explains, in their simulations, higher yields for OD photodesorption with respect to OH and the independence with surface temperature. Whereas OD photodesorption is twice that of OH in the theoretical study, the differential desorption appears to be much more dramatic in the experimental data, in which OH signal is hardly decoupled from the noise level. A recent molecular dynamics study of the energy dissipation on crystalline water ice surface which investigates the role of the initial kinetic energy on desorption probabilities clearly points out the presence of a threshold energy for desorption to occur (Fredon et al. 2017), which is linked to the interaction energy between the desorbing species and the surface. The interaction energy of radicals in water clusters (5 water molecules) were calculated around 0.26 eV, a value which is above the available kinetic energy for OH (0.142 eV) (Allodi et al. 2006). Other quantum mechanics approaches (Own N-layer Integrated molecular Orbital Molecular Mechanic) applied to OH interacting on hexagonal water ice found a range of binding energies from 0.2 eV to 0.67 eV depending on the binding sites and the orientation of the OH radical. This set of binding energies are higher than the available kinetic energy for OH. A broad range of binding energies can be expected on compact amorphous water ice as well. We suggest that the kinetic energy of most OH radicals is not sufficient to overcome their barrier, reducing drastically the desorption probability. Simultaneously, more OH photofragments, as compared to OD, remained at surface or in the ice and a part of them would be available for non-thermal surface reactions, thus resulting in $\text{H}_2\text{O}/\text{D}_2\text{O} > 1$, as observed. The OD desorption yields from D_2O irradiation at 8.5 eV is 3×10^{-4} molecule/photon at 15 K a value similar to the H_2O yields (Fig. 7). This effect could thus account for a large part of the H_2O desorption, assuming most of the OH radicals are converted back to (desorbing) water molecules, and could contribute to the differences observed between H_2O and D_2O .

The desorption yields of water was previously estimated by different groups using microwave hydrogen discharge lamps. Westley et al. (1995b) reported a value of 3.5×10^{-3} molecule/photon at 35 K and Öberg et al. (2009) derived a value of 2×10^{-3} molecule/photon at 20 K. Assuming that most of the photon flux was at Ly- α emission, these values can be compared to the yields measured at 10 eV in the present study, that is $(7 \pm 1) \times 10^{-4}$ molecule/photon and $(8 \pm 1) \times 10^{-5}$ molecule/photon for H₂O and D₂O at 15 K respectively. As pointed-out by Cruz-Diaz et al. (2018), this apparent discrepancy is due to the experimental methods used in these previous studies (quartz crystal microbalance and infrared spectroscopy) that are both probing the photodesorption of water through its destruction, making difficult to separate the contribution of intact water desorption from other sources of water depletion from the solid phase (desorption as photofragments, photodissociation without desorption, chemical reaction at surface and within the bulk). DeSimone et al. (2013) estimated a H₂O photodesorption yield of 1.8×10^{-4} molecule/photon from ASW at 108 K after laser irradiation at 7.9 eV (157 nm) and direct detection into the gas phase by time-of-flight spectroscopy, a value in very close agreement with this study which gives $(2.6 \pm 0.3) \times 10^{-4}$ molecule/photon at 8 eV. Cruz-Diaz et al. (2018) recently reported new photodesorption yields after irradiation of ASW with a broad band microwave hydrogen plasma lamp and detection of water into the gas phase with a calibrated QMS, a detection method similar to the one used in the present study. Although a precise comparison would require to take into account the spectra profile of the lamp, the comparison reveals a gap between the two sets of data. At low temperatures (< 40 K) they differ by a factor ~ 1.8 for H₂O, which is remarkably small, but by almost one order of magnitude for D₂O. The fact that the ratio are different between the two isotopologues suggests that the differences between the two groups can not simply be assigned to a shift in the absolute yields obtained after QMS calibration which would give a systematic gap (although this could account for a factor of 2 typically). Also we point out the temperature dependence of the yields are different, since yields obtained in Cruz-Diaz et al. (2018) increase significantly above 50 K, whereas that obtained in this work start increasing above ~ 70 K. These two distinct thermal evolutions could be explained by two distinct sample morphologies. Indeed, the water ice samples are prepared at 100 K in the present study, producing compact and stable ASW, and they are prepared at 8 K in Cruz-Diaz et al. (2018) and subsequently warmed up to the irradiation temperature, leading to highly porous ASW low density samples, with a morphology sensitive to the temperature due to pore collapse. In porous-ASW, surface water molecules with low coordination number are more likely formed as compared to compact ASW and are distributed over a much larger surface area. These weakly bound species may also more easily desorb and contribute to higher desorption signal. It is generally assumed that compact forms of water are more relevant under interstellar conditions, in particular because of compaction induced by cosmic ion bombardment and VUV irradiation (Palumbo 2006; Mejía et al. 2015; Palumbo et al. 2010). Regardless, the differences observed between the two studies are still surprisingly high for D₂O and the role played by surface roughness is not easily predictable. This calls into question the role of the surface morphology in the relative contributions of the desorption mechanisms for water, and its consequence on fractionation. Indeed, molecular dynamics study have shown higher desorption probabilities of OH radicals from crystalline ice than from amorphous ice for example (Andersson et al. 2006), a difference which may affect water

desorption as discussed above. It would be interesting to get a better estimate of the sensitivity of these desorption yields with the surface morphology in the experiments.

4.2. Desorption of molecular hydrogen and molecular oxygen

Although the formation and desorption of H₂ (D₂) and O₂ from the initial irradiation of water ice are not driven exactly by the same chemical pathways, they share common properties, resulting both from rapid diffusion of excitons to -or near- the surface of ASW. The production of molecular hydrogen from water ice can arise (a) directly from water photodissociation giving H₂ and O, or (b) indirectly by water photodissociation producing H and OH fragments followed by H atom recombination and/or H abstraction reactions with H₂O (Watanabe et al. 2000). In the gas phase, the first electronic excited state is purely dissociative. In the condensed phase, H atoms can recombine with OH to form H₂O, limiting therefore the efficiency of water destruction within the bulk (cage effect), but not in the same way at the surface where the excited molecules are not entirely surrounded by the water matrix. Molecular hydrogen released into the gas phase in highly excited states ($v = 0-5$; $J = 0-17$) has been detected after irradiation of 100 K ASW and polycrystalline ice, after excitation in the red-tail of the absorption band (193 nm, 157 nm) (Yabushita et al. 2008b,a). The translational and rovibrational energy partition is consistent with the indirect mechanisms, with substantial internal excitation in the case of the recombination reaction, and low translational and rovibrational energy in the case of abstraction reaction. The production of molecular hydrogen from amorphous solid water films on Pt(111) observed from electron-stimulated desorption (ESD) provides evidence for rapid migration of the electronic excitation deposited in the ASW film from the bulk to the ASW vacuum interface (Petrik & Kimmel 2003, 2004). The results thus suggest the molecules are produced at the interfaces of ASW and not from the interior of the film.

All these processes occurring at the surface of ASW are initiated by the photodissociation of water. The photodesorption yields of these fragments thus reflect the initial photodissociation efficiency. Assuming the photodesorption yields are proportional to the photodissociation efficiency, one can deduce from the shape of PSD spectra that most of the photodissociation occurs in the first absorption band, peaking around 9 eV, and that photodissociation cross sections are decreasing above 10 eV, despite the increase of the absorption cross sections at high energy (Fig. 4).

Concerning molecular oxygen, O₂ ($X^3\Sigma_g^-$) and O₂ ($a^1\Delta_g$) desorption have been observed from ASW at 90 K (Hama et al. 2010a) in the 157 nm laser irradiation experiment. The formation mechanism proposed involve O (3P) atoms which react with OH to form O₂. O (3P) atoms could arise from the recombination of two OH radicals or from the photodissociation of H₂O₂. Molecular oxygen originates from successive surface reactions where OH radicals are playing a central role. The ESD of molecular oxygen from amorphous solid water has also been subject of detailed investigations (Petrik et al. 2006b,a). The ESD experimental results could be reproduced with a kinetic model involving a multistep reactions sequence. In this scheme, OH radicals produced by the relaxation of the electronic excitation at the surface of ASW recombine to form H₂O₂, which reacts itself with OH to produce HO₂. HO₂ is believed to be the precursor of O₂ through a subsequent reaction with another species (most probably with OH arising from H₂O dissociation). One can note the central role

again played by mobile OH radicals at or near ASW vacuum interface, in all the above chemical schemes leading to O₂. The fact that we observe a strong dependence of O₂ photodesorption yields with irradiation time is consistent with the accumulation of OH and H₂O₂ photoproducts on the surface and with these types of secondary chemistry. It is also true for our measured temperature dependence of O₂ desorption (see the next section).

4.3. Temperature effects

Both molecular hydrogen and molecular oxygen are secondary processes initiated by successive photodissociation events. At low temperature and following the pictures given in the previous section, these molecules are believed to be formed near or at the ASW/vacuum interface. The desorption of these two molecules is significantly enhanced at high temperatures. This increase can not be assigned to enhanced surface diffusion. Indeed, at high temperature, the residence time of the particles are greatly reduced, limiting therefore the probability of reaction. This competition between diffusion and desorption is known for example to explain why the formation of molecular hydrogen via the Langmuir-Hinshelwood mechanism is efficient in a tiny range of temperatures (Vidali 2013). Consequently, higher photodesorption yields are not explained by phenomena occurring entirely at the external surface of the sample, but must involve particles originating underneath. The fact that all the desorbing species present a threshold in the same temperature range around ~ 60-80 K, as shown in Fig. 6 suggests an origin linked to the water matrix itself. Indeed, the diffusion of species within the water ice network has been shown to be similar to self-water diffusion inside the matrix, due to the fact that diffusion is governed by ice restructuration (Ghesquière et al. 2018). ASW crystallizes to cubic ice above 125 K. Below 100 K, ASW is continuously evolving. The morphology of porous ASW samples investigated by infrared spectroscopy which probes the dangling OH bonds at the surface of micropores have shown evidence for ice restructuration near 75-80 K (Rowland et al. 1991). Although the experimental protocol used in the present experiment leads to the production of compact structures that are expected to be nonporous, (Stevenson et al. 1999), Rowland et al. (1991) study suggests that the ice matrix gets sufficient energy to transform around 80 K. This would allow the atoms and molecules trapped underneath the surface to gain mobility, react and/or reach the external surface of the sample. One can note in addition that thermal desorption of H₂ and O₂ occurs around 10-20 K and ~30 K respectively. Any of these molecules reaching the surface above 70 K would thus promptly desorb without the need of non-thermal energy. By contrast, thermal desorption of water isn't efficient even at 110 K and exothermic events near the surface of the sample are still required to account for intact water desorption. In other words, the stronger enhancement of O₂ and H₂ (D₂) as compared to water, can be explained by a desorption thermally supported for the most volatiles species.

4.4. Astrophysical implications

The HDO/H₂O and D₂O/HDO abundance ratios derived from observations in star forming regions are good tracers of water formation. Indeed, these ratios are used to follow the water trail all along the way from the prestellar stage up to the formation of disks, planetesimals and planets, and provide valuable keys to try to understand to what extent molecules formed in interstellar clouds can be preserved (van Dishoeck et al. 2014; Ceccarelli

et al. 2014). The D₂O/HDO ratio, in particular, has been shown to be a pertinent probe of the origin of water into protostellar disks (Furuya et al. 2017), giving some indication of a presolar origin of water in 67P comet (Altwegg et al. 2019). Quantitative predictions provided by astrochemical models are thus crucial to interpret the isotopic abundances. In this context it is important to provide good laboratory data and to understand how the photodesorption could affect fractionation.

In this experimental study, we have explored the absolute photodesorption yields of water on a wide energy range relevant to star-forming regions. This provides the first complete picture of the yields variation in the VUV. Concerning D₂O, photodesorption yields from D₂O diluted into H₂O-rich ice would have been required to be fully relevant to interstellar conditions. However Koning et al. (2013) have shown that the desorption probabilities of D₂O embedded in H₂O ice are in fact very similar to that of D₂O in D₂O ice at any temperature. This indicates that the effect of the kick-out and recombination mechanisms are similar for both systems. Although, it is not known how the potential electronic relaxation (MGR model) contribution would change in the case of D₂O molecules embedded into an H₂O matrix, we believe that our measurements provide valuable estimates of D₂O photodesorption yields. One should also keep in mind the high range of values associated to these measurements of photodesorption yields, as attested by the deviations observed between different experimental studies (up to one order of magnitude), as mentioned in the previous section.

In order to take into account the variation of the photodesorption efficiency with photon energy over the 7-13.5 eV energy range, new photodesorption yields have been calculated for both systems by taking into account the spectral profiles of the Interstellar Standard Radiation Field (ISRF) and that of secondary emission induced by cosmic rays. The results are shown in table 1, which includes in addition the yields for an excitation at 10 eV (~ Ly- α) for comparison. The sensitivity of the yields to different spectral profiles is limited because the maximum of photodesorption lies at Ly- α energy corresponding to the main emission induced by cosmic rays and because the ISRF profile is relatively flat in this energy range. We recommend to use in astrochemical models 5×10^{-4} molecule/photon at low temperatures (< 60 K) for intact H₂O. More precisely, we found that the temperature dependence above 60 K can be described by a simple linear function of the temperature T (in Kelvin). The photodesorption yields for H₂O are :

$$Y(T) = 5 \times 10^{-4} \text{ molecule/photon } (T \leq 60 \text{ K})$$

$$Y(T) = 5 \times 10^{-4} + 1.1 \times 10^{-5} \times (T - 60) \text{ molecule/photon} \\ (60 \text{ K} < T \leq 110 \text{ K}) \quad (3)$$

The corresponding D₂O photodesorption yields can be described by the same law but must be divided by 10.

The determination of isotopic abundances in the solid phase of water in observations is very difficult due to the low-level of absorption signals from amorphous ice mantles (Dartois et al. 2003) and the presence of other solid-phase interstellar molecule vibrational features close to the O-D stretching mode band frequency (Urso et al. 2018). Besides, the observations of gas-phase D₂O remain very scarce and difficult (Coutens et al. 2014). It is therefore important to know whether the abundances ratio measured in the gas phase would reflect that in the solid phase. The present results show that in cold regions where the UV photodesorption dominates the gas phase water abundances, the H₂O/D₂O abundances ratio measured in the gas phase is not reflecting

Table 1. VUV photodesorption yields ($\times 10^{-4}$ molecule/photon) of water from c-ASW. ^afrom Mathis et al. (1983) ; ^bfrom Gredel et al. (1987)

Energy (eV)	15 K	100 K	15 K	100 K
	H ₂ O	H ₂ O	D ₂ O	D ₂ O
ISRF ^a	4.0 ± 0.7	6.1 ± 0.7	0.4 ± 0.1	0.7 ± 0.1
Second. UV ^b	5.5 ± 0.9	7.6 ± 0.9	0.6 ± 0.1	0.9 ± 0.1
10.2 eV (Ly- α)	6.7 ± 1.3	8.8 ± 1.0	0.8 ± 0.1	1.0 ± 0.2

directly that of the solid phase value because the photodesorption yields largely differ.

The experimental study of HDO photodesorption is very challenging and has not been addressed here. Regarding the electronic relaxation model (MGR), the desorption probability of HDO would give lower desorption when the O-D stretch mode is initially excited as compared to O-H, which statistically results in a lower desorption probability of HDO as compared to H₂O. Considering the chemical recombination route, this study shows that depending on their kinetic energy, the hydroxyl radicals OX (X=H or D) promptly desorb following water photodissociation or remain in the solid and lead to X₂O desorption. In HDO, by contrast with the relative behavior between H₂O and D₂O photodissociation, it is the OH fragments which gain more kinetic energy upon HDO photodissociation as compared to OD photofragments, which should result (by extrapolation of our result) to a differential photodesorption of OH as compared to OD radicals. This effect is modulated by the HDO photodissociation branching ratio, which gives two (H+OD) fragments for one (D+OH) fragments (Koning et al. 2013). Thus, regarding the chemical recombination route, we predict the photodesorption of HDO to be 2/3 that of H₂O. Both channels (electronic relaxation and chemical recombination) are thus contributing to deuterium fractionation, although these effects remain small considering the relatively low fractionation in water ices derived from IR observations (HDO/H₂O $\lesssim 10^{-2}$) (Parise et al. 2003; Dartois et al. 2003). Recent progresses in physical and astrochemical models have provided consistent scenarios explaining the evolution of the HDO/H₂O and D₂O/HDO ratio at the early stage of molecular clouds, in protostellar cores (Taquet et al. 2014; Furuya et al. 2015, 2016; Kalvāns et al. 2017) and during the incorporation of water into disks (Furuya et al. 2017). As initially proposed by Dartois et al. (2003) and further demonstrated in recent models, H₂O is formed primarily at the early stages of molecular clouds, whereas HDO and D₂O are mostly formed later in the very cold and high density stage, where UV irradiation is less effective and the top layers of ice mantle enriched with many other species (CO, CO₂, CH₃OH, NH₃ etc.). Thus, electronic relation and/or chemical recombination could impact the ice mantle composition during its growth, favoring the fractionation in its bulk. Regarding the highly deuterated top layers of the mantle, as our results suggest that the photodesorption of water is critically sensitive to the surface morphology and composition, the role played by water photodesorption from such complex chemical environment still needs to be studied to better constrain its effect on fractionation.

In this study, we found that at least 86% of H₂O desorbs as intact water and not as OH+H photofragments : contrary to what is generally assumed, we found the OH photodesorption yield is weak. This finding is paramount for the chemistry in the comet-formation region of protoplanetary disks. Indeed, using time-

dependent gas-grain chemical model in a region of a T-Tauri disk corresponding likely to comet-formation, Chaparro Molano & Kamp (2012) have shown that secondary VUV (induced by cosmic rays) photodesorption from water ice delivers highly reactive OH radicals into the gas phase. This pathway opens new gas phase chemical routes that change the chemical balance and the final abundances, enabling in particular oxygen to be distributed in O₂, SiO and atomic oxygen, and carbon to be stored in CO and CO₂. As our results show that much less OH is produced by photodesorption than previously calculated, the model predicts that in poor-OH environment, most of oxygen will be found in H₂O, CO and CO₂ and a fraction of carbon in CH₄, which matches much better the cometary composition. Also it is important to note that the production OH radicals into the gas phase arising from water ice photodesorption does not reflect that of direct gas phase photodissociation, which can give large errors in the estimates of photodesorption yields derived from gas phase photodissociation cross sections data (Fogel et al. 2011).

5. Conclusion

The photodesorption yields of H₂O, OH, H₂ and O₂ from amorphous H₂O ices, D₂O, OD, D₂ and O₂ from amorphous D₂O ices, have been measured from 7 to 13.5 eV and for sample temperatures between 15-110 K. This provides the first photon-energy dependence of the photodesorption yields in the vacuum-UV. The yields were found to increase rapidly from 7 to 10 eV and to decrease at higher energies. For intact water desorption, the maximum desorption yields are found in the second exciton band around 10 eV.

The desorption at low (15 K) and high (100 K) temperatures present very similar photon energy dependence for all species, with the exception of hydroxyl radicals. For the desorption of H₂O (D₂O), and to a greater extent that of H₂ (D₂) and O₂, we observe a dramatic enhancement above (70±10) K. This effect is assigned to the contribution from material originating deeper underneath the surface contributing to the chemical processes at higher temperatures including desorption induced by exothermic reactions for H₂O and D₂O, along with desorption thermally assisted for the lighter species.

The recommended H₂O photodesorption yields over the VUV range are (5±2)×10⁻⁴ molecule/photon from compact ASW at low temperature (15 K) and increase linearly above 60 K with a rate of 1.1×10⁻⁵ molecule/photon/K. The corresponding D₂O photodesorption yields were found to be ten times lower. The relative desorption of OH/OD photofragments, associated to direct photodissociation are anti-correlated to that of H₂O/D₂O. These effects can be explained by a differential chemical recombination involving OH (OD) photofragments and/or possibly by a Menzel-Gomer-Redhead isotope effect in desorption. In the former case, we suggest that the trapping of OH photofragments on our c-ASW sample is converted into H₂O desorption, a process making the relative weights of the photodesorption channels sensitive to the isotopic composition and surface morphology. This process could contribute to increase the HDO/H₂O ratios in the solid phase during the build-up of the water ice mantles in molecular clouds and to favor adequate chemical environment for oxygen bearing molecules in comet-forming regions of protoplanetary disks.

Acknowledgements. We acknowledge SOLEIL for provision of synchrotron radiation facilities under the projects 20150760 and 20180060. We thank Laurent Nahon and the DESIRS team for their assistance on the beamline. This study was supported by the Programme National Physique et Chimie du Milieu Interstellaire (PCMI) of CNRS/INSU with INC/INP co-funded by CEA and

CNES. It was done in collaboration and with financial support by the European Organization for Nuclear Research (CERN) under the collaboration agreement KE3324/TE. Financial support from the LabEx MiChem, part of the French state funds managed by the ANR within the investissements d'avenir program under reference ANR-11-10EX-0004-02, and by the Ile-de-France region DIM ACAV program, is gratefully acknowledged.

References

- Aikawa, Y. & Herbst, E. 1999, *Astronomy & Astrophysics*, 351, 233
- Allodi, M. A., Dunn, M. E., Livada, J., Kirschner, K. N., & Shields, G. C. 2006, *Journal of Physical Chemistry A*, 110, 13283
- Altwegg, K., Balsiger, H., & Fuselier, S. A. 2019, *Annu. Rev. Astron. Astrophys.*, 57, 113
- Andersson, S., Al-Halabi, A., Kroes, G.-J., & van Dishoeck, E. F. 2006, *The Journal of Chemical Physics*, 124, 064715
- Andersson, S., Arasa, C., Yabushita, A., et al. 2011, *Phys. Chem. Chem. Phys.*, 13, 15810
- Andersson, S., Kroes, G.-J., & van Dishoeck, E. F. 2005, *Chemical Physics Letters*, 408, 415
- Andersson, S. & van Dishoeck, E. F. 2008, *A&A*, 491, 907
- Arasa, C., Andersson, S., Cuppen, H. M., van Dishoeck, E. F., & Kroes, G.-J. 2010, *The Journal of Chemical Physics*, 132, 184510
- Arasa, C., Andersson, S., Cuppen, H. M., van Dishoeck, E. F., & Kroes, G. J. 2011, *The Journal of Chemical Physics*, 134, 164503
- Arasa, C., Koning, J., Kroes, G.-J., Walsh, C., & van Dishoeck, E. F. 2015, *A&A*, 575, A121
- Öberg, K. I., Linnartz, H., Visser, R., & van Dishoeck, E. F. 2009, *ApJ*, 693, 1209
- Bergeld, J. & Chakarov, D. 2006, *The Journal of Chemical Physics*, 125, 141103
- Bertin, M., Fayolle, E. C., Romanzin, C., et al. 2013, *Astrophys. J.*, 779, 120
- Caselli, P., Keto, E., Bergin, E. A., et al. 2012, *The Astrophysical Journal*, 759, L37
- Cazaux, S., Minissale, M., Dulieu, F., & Hocuk, S. 2016, *Astronomy & Astrophysics*, 585, A55
- Ceccarelli, C., Caselli, P., Boekelee-Morvan, D., et al. 2014, *Protostars and Planets VI*, University of Arizona Press, 869
- Chaparro Molano, G. & Kamp, I. 2012, *A&A*, 537, A138
- Ciesla, F. J. 2014, *ApJ*, 784, L1
- Coutens, A., Jørgensen, J. K., Persson, M. V., et al. 2014, *ApJ*, 792, L5
- Crouse, J., Loock, H.-P., & Cann, N. M. 2015, *The Journal of Chemical Physics*, 143, 034502
- Cruz-Diaz, G. A., Caro, G. M. M., & Chen, Y.-J. 2014a, *Monthly Notices of the Royal Astronomical Society*, 439, 2370
- Cruz-Diaz, G. A., Martín-Doménech, R., Moreno, E., Muñoz Caro, G. M., & Chen, Y.-J. 2018, *Monthly Notices of the Royal Astronomical Society*, 474, 3080
- Cruz-Diaz, G. A., Muñoz Caro, G. M., Chen, Y.-J., & Yih, T.-S. 2014b, *A&A*, 562, A119
- Dartois, E., Augé, B., Boduch, P., et al. 2015, *A&A*, 576, A125
- Dartois, E., Chabot, M., Id Barkach, T., et al. 2018, *A&A*, 618, A173
- Dartois, E., Thi, W.-F., Geballe, T. R., et al. 2003, *A&A*, 399, 1009
- DeSimone, A. J., Crowell, V. D., Sherrill, C. D., & Orlando, T. M. 2013, *The Journal of Chemical Physics*, 139, 164702
- DeSimone, A. J. & Orlando, T. M. 2014, *The Journal of Chemical Physics*, 140, 094702
- DeSimone, A. J. & Orlando, T. M. 2015, *Icarus*, 255, 44
- Doronin, M., Bertin, M., Michaut, X., Philippe, L., & Fillion, J.-H. 2015, *Journal of Chemical Physics*, 143, 084703
- Dupuy, R., Bertin, M., Féraud, G., et al. 2018, *Nat Astron.*, 2, 796
- Dupuy, R., Féraud, G., Bertin, M., et al. 2017, *A&A*, 606, L9
- Es-sebbar, E.-t., Bénilan, Y., Fray, N., et al. 2015, *ApJS*, 218, 19
- Fayolle, E. C., Bertin, M., Romanzin, C., et al. 2011, *The Astrophysical Journal*, 739, L36
- Fayolle, E. C., Bertin, M., Romanzin, C., et al. 2013, *Astron. Astrophys.*, 556, A122
- Fillion, J.-H., Amiaud, L., Congiu, E., et al. 2009, *Phys. Chem. Chem. Phys.*, 11, 4396
- Fillion, J.-H., Fayolle, E. C., Michaut, X., et al. 2014, *Faraday Discussions*, 168, 533
- Fillion, J. H., van Harreveld, R., Ruiz, J., et al. 2001, *J. Phys. Chem. A*, 105, 11414
- Fogel, J. K. J., Bethell, T. J., Bergin, E. A., Calvet, N., & Semenov, D. 2011, *ApJ*, 726, 29
- Fredon, A., Lamberts, T., & Cuppen, H. M. 2017, *ApJ*, 849, 125
- Furuya, K., Aikawa, Y., Hincelin, U., et al. 2015, *A&A*, 584, A124
- Furuya, K., Drozdovskaya, M. N., Visser, R., et al. 2017, *A&A*, 599, A40
- Furuya, K., van Dishoeck, E. F., & Aikawa, Y. 2016, *A&A*, 586, A127
- Ghesquière, P., Ivlev, A., Noble, J. A., & Theulé, P. 2018, *A&A*, 614, A107
- Gredel, G., Lepp, S., & Dalgarno, A. 1987, *The Astrophysical Journal*, 323, L137
- Hama, T., Yabushita, A., Yokoyama, M., Kawasaki, M., & Watanabe, N. 2009, *The Journal of Chemical Physics*, 131, 114510
- Hama, T., Yokoyama, M., Yabushita, A., & Kawasaki, M. 2010a, *The Journal of Chemical Physics*, 133, 104504
- Hama, T., Yokoyama, M., Yabushita, A., et al. 2010b, *The Journal of Chemical Physics*, 132, 164508
- Hogerheijde, M. R., Bergin, E. A., Brinch, C., et al. 2011, *Science*, 334, 338
- Hollenbach, D., Kaufman, M. J., Bergin, E. A., & Melnick, G. J. 2009, *The Astrophysical Journal*, 690, 1497
- Jenniskens, P., Blake, D. F., Wilson, M. A., & Pohorille, A. 1995, *The Astrophysical Journal*, 455, 389
- Kalvāns, J., Shmeld, I., Kalnin, J. R., & Hocuk, S. 2017, *Mon. Not. R. Astron. Soc.*, 467, 1763
- Kamp, I., Thi, W.-F., Meeus, G., et al. 2013, *A&A*, 559, A24
- Kimmel, G. A., Stevenson, K. P., Dohnálek, Z., Smith, R. S., & Kay, B. D. 2001, *The Journal of Chemical Physics*, 114, 5284
- Kobayashi, K. 1983, *Journal of Physical Chemistry*, 87, 4317
- Koning, J., Kroes, G. J., & Arasa, C. 2013, *The Journal of Chemical Physics*, 138, 104701
- Mathis, J., Mezger, P., & Panagia, N. 1983, *Astronomy & Astrophysics*, 128, 212
- Mejía, C., de Barros, A., Seperuelo Duarte, E., et al. 2015, *Icarus*, 250, 222
- Muñoz Caro, G. M. & Schutte, W. A. 2003, *A&A*, 412, 121
- Nahon, L., de Oliveira, N., Garcia, G. A., et al. 2012, *J Synchrotron Rad.*, 19, 508
- Nishi, N., Shinohara, Hisanori, & Okuyama, Tohru. 1984, *The journal of chemical physics*, 80, 3898
- Palumbo, M., Baratta, G., Leto, G., & Strazzulla, G. 2010, *Journal of Molecular Structure*, 972, 64
- Palumbo, M. E. 2006, *A&A*, 453, 903
- Parise, B., Simon, T., Caux, E., et al. 2003, *A&A*, 410, 897
- Petrik, N. G., Kavetsky, A. G., & Kimmel, G. A. 2006a, *J. Phys. Chem. B*, 110, 2723
- Petrik, N. G., Kavetsky, A. G., & Kimmel, G. A. 2006b, *The Journal of Chemical Physics*, 125, 124702
- Petrik, N. G. & Kimmel, G. A. 2003, *Phys. Rev. Lett.*, 90, 166102
- Petrik, N. G. & Kimmel, G. A. 2004, *J. Chem. Phys.*, 121, 10
- Putaud, T., Michaut, X., Le Petit, F., Roueff, E., & Lis, D. C. 2019, *A&A*, 632, A8
- Ramsier, R. & Yates, J. 1991, *Surface Science Reports*, 12, 246
- Rowland, B., Fisher, M., & Devlin, J. P. 1991, *The Journal of Chemical Physics*, 95, 1378
- Salinas, V. N., Hogerheijde, M. R., Bergin, E. A., et al. 2016, *A&A*, 591, A122
- Stevenson, K. P., Kimmel, G. A., Dohnálek, Z., Smith, R. S., & Kay, B. D. 1999, *Science*, 283, 1505
- Straub, H. C., Lindsay, B. G., Smith, K. A., & Stebbings, R. F. 1998, *The Journal of Chemical Physics*, 108, 109
- Taquet, V., Charnley, S. B., & Sipilä, O. 2014, *ApJ*, 791, 1
- Terada, H. & Tokunaga, A. T. 2017, *ApJ*, 834, 115
- Urso, R. G., Palumbo, M. E., Baratta, G. A., Scirè, C., & Strazzulla, G. 2018, *Monthly Notices of the Royal Astronomical Society*, 479, 130
- van Dishoeck, E. F., Bergin, E. A., Lis, D. C., & Lunine, J. I. 2014, *Protostars and Planets VI*, University of Arizona Press, 835
- Vidali, G. 2013, *Chem. Rev.*, 21
- Walsh, C., Millar, T. J., & Nomura, H. 2010, *The Astrophysical Journal*, 722, 1607
- Watanabe, Horii, & Kouchi. 2000, *The Astrophysical Journal*, 541, 771
- Westley, M., Baragiola, R., Johnson, R., & Baratta, G. 1995a, *Planetary and Space Science*, 43, 1311
- Westley, M. S., Baragiola, R. A., Johnson, R. E., & Baratta, G. A. 1995b, *Letters to Nature*, 373, 405
- Willacy, K. & Langer, W. D. 2000, *The Astrophysical Journal*, 544, 903
- Wolf, M., Nettesheim, S., White, J. M., Hasselbrink, E., & Ertl, G. 1991, *The Journal of Chemical Physics*, 94, 4609
- Yabushita, A., Hama, T., Iida, D., et al. 2008a, *The Astrophysical Journal*, 682, L69
- Yabushita, A., Hama, T., Iida, D., et al. 2008b, *The Journal of Chemical Physics*, 129, 044501
- Yabushita, A., Hama, T., & Kawasaki, M. 2013, *Journal of Photochemistry and Photobiology C: Photochemistry Reviews*, 16, 46
- Yabushita, A., Hama, T., Yokoyama, M., et al. 2009, *ApJ*, 699, L80
- Zhang, Z., Piatkowski, L., Bakker, H. J., & Bonn, M. 2011, *Nature Chem.*, 3, 888
- Zhu, X.-Y. & White, J. M. 1992, *Phys. Rev. Lett.*, 68, 3359